mater.scichina.com link.springer.com https://doi.org/10.1007/s40843-025-3506-3

Self-supported partially crystallized nanoporous metallic glass for ultra-stable and efficient electrocatalytic hydrogen evolution

Jihan Jiang[1], Wenqing Ruan[1*], Shenghao Zeng[1], Jiaqing Lin[1], Xingran Zhao[1], Jianan Fu[2], Qing Chen[3], Xiaodi Liu[1*] and Jiang Ma[1*]

ABSTRACT Metallic glasses (MGs) often suffer from sluggish hydrogen evolution reaction (HER) kinetics in neutral and alkaline media, with their catalytic performance predominantly confined to acidic environments. Herein, we reported a novel thermoplastic forming technique to fabricate a self-supported partially crystallized nanoporous $Pt_{56.2}Ni_{5.2}Cu_{16.8}P_{21.8}$ metallic glass (C-NPMG). The C-NPMG catalyst delivers ultralow overpotentials of 18.0 mV (0.5 M H_2SO_4), 42.2 mV (1 M KOH), and 88.0 mV (1 M phosphate-buffered saline (PBS)) at a current density of 10 mA cm^{-2}, outperforming most state-of-the-art non-noble MGs and Pt-based benchmarks across all pH conditions. Notably, it maintains negligible performance decay for over 1000 h in alkaline electrolytes, showcasing superior stability. Experimental and computational analyses reveal that the enhanced HER activity arises from three synergistic effects: (1) the high-specific-surface-area nanoporous architecture that maximizes active site exposure; (2) the formation of crystallite-amorphous interfaces during partial crystallization, which lowers the energy barrier for H_2 desorption; (3) the hierarchical super-hydrophilic and super-hydrophobic wettability of the C-NPMG, which optimizes mass transport and prevents electrolyte-induced corrosion. This work establishes a novel design paradigm for developing high-performance, pH-universal HER electrocatalysts by integrating structural nano-engineering and crystallite-amorphous phase synergy in metallic glass systems to overcome the trade-offs between performance and stability in electrochemical water splitting.

Keywords: metallic glass, thermoplastic forming, self-supported nanoporous structure, hydrogen evolution reaction

INTRODUCTION

The escalating consumption of fossil fuels and the concomitant environmental degradation have underscored the urgency of developing sustainable energy technologies [1,2]. Hydrogen (H_2), with its unmatched energy density (120 MJ kg^{-1}) and carbon-neutral lifecycle, emerges as a pivotal candidate for decarbonized energy systems [3,4]. Among various H_2 production routes, electrochemical water splitting stands out for its scalability and compatibility with renewable energy integration, enabling efficient conversion of electrical energy into storable chemical energy [5]. Central to this technology is the hydrogen evolution reaction (HER) at the cathode, where the development of high-performance catalysts with low overpotential, broad pH adaptability, and exceptional durability remains a critical challenge.

Conventional HER catalysts, including noble-metal-based catalysts (e.g., Pt nanoparticles), exhibit superior activity in acidic media but suffer from sluggish kinetics in neutral and alkaline electrolytes due to the energy-intensive water dissociation step and unfavorable hydrogen adsorption-desorption dynamics [6,7]. For instance, the hydrogen binding energy on Pt surfaces deviates from the optimal range in alkaline environments, leading to a two to three order of magnitude activity decline compared to acidic conditions [8]. While non-noble metal catalysts (e.g., NiMo, transition metal dichalcogenides) offer cost advantages, their stability and pH universality remain inadequate for practical applications [9–11]. Moreover, most state-of-the-art catalysts are powder-based, requiring complex binder-assisted electrode fabrication that often results in active site burial, poor electron transport, and structural degradation during operation [12,13].

Metallic glasses (MGs), characterized by their disordered atomic structure and tunable physicochemical properties, have emerged as promising candidates for electrocatalysis [14]. Their amorphous matrix provides abundant unsaturated coordination sites and resistance to chemical corrosion, while compositional flexibility allows rational design of catalytically active surfaces. However, the HER performance of MGs is typically constrained by their limited specific surface area and suboptimal hydrogen adsorption energy in non-acidic media [15]. Strategies to enhance MGs-based catalysts, such as compositional doping [16], or surface nanostructuring via electrochemical dealloying [17], template electrodeposition [18], and magnetron sputtering [19,20] have been used to increase the electrode surface area and create nanostructures on MG surfaces. However, these methods are more involved and time-consuming.

Herein, leveraging the unique thermoplastic formability of MGs in the supercooled liquid region (SLR), where their viscosity decreases drastically under combined thermal and mechanical stimuli, enables rapid fabrication of self-supported nanoporous structures with minimal energy input [21,22]. This

[1] Shenzhen Key Laboratory of High Performance Nontraditional Manufacturing, College of Mechatronics and Control Engineering, Shenzhen University, Shenzhen 518060, China
[2] Department of Mechanics and Aerospace Engineering, Southern University of Science and Technology, Shenzhen 518055, China
[3] Department of Mechanical and Aerospace Engineering, The Hong Kong University of Science and Technology, Hong Kong 999077, China
* Corresponding author (email: ruanwq@szu.edu.cn; xdliu2018@szu.edu.cn; majiang@szu.edu.cn)

can be used to quickly and easily prepare self-supported nanoporous structures on the surface of MGs [23,24], which can significantly increase their defect abundance and specific surface area [25,26] and provide more catalytically active sites, all of which can improve HER performance.

This work introduces a scalable thermoplastic processing approach using as-cast Pt-based MG thin ribbons as precursors, enabling efficient fabrication with minimized steps and significantly enhancing Pt utilization, reducing catalyst mass by over 95% relative to bulk counterparts (Fig. S1) [27]. The synergistic interplay of (i) a nanoporous architecture with high specific surface area (maximizing active site exposure), (ii) crystallite-amorphous interfaces lowering H_2 desorption energy barriers (ΔG_{H^*} reduced by 0.287 eV), and (iii) a hierarchically super-hydrophilic and super-hydrophobic surface (optimizing mass transport and durability) endows the partially crystallized nanoporous Pt-based MG (C-NPMG) with exceptional pH-universal HER activity. This integrated design paves the way for scalable production of high-performance electrocatalysts by leveraging structural nano-engineering and phase synergy in MG systems.

RESULTS AND DISCUSSION

Fabrication and structural characterization of C-NPMG

The catalyst nomenclature in this study is systematically defined by its elemental composition, determined via inductively coupled plasma optical emission spectroscopy (ICP-OES) to ensure a precise correlation between chemical makeup and material properties. The precursor material is an MG ribbon with a nominal composition of $Pt_{56.2}Ni_{5.22}Cu_{16.8}P_{21.8}$ (at%) (Fig. S3), selected for its optimal Pt content to balance electrocatalytic activity and cost efficiency, while also ensuring the glass-forming ability to maintain the amorphous matrix, in line with prior research on Pt-based alloy catalysts for HER [28]. Differential scanning calorimetry (DSC) analysis of the as-cast MG ribbon confirms its amorphous nature, revealing a glass transition temperature (T_g) of 227.44 °C and a crystallization temperature (T_x) of 288.04 °C, yielding a wide supercooled liquid region (SLR: $\Delta T = T_x - T_g = 60.6$ °C) (Fig. 1b). This thermodynamic characteristic is critical for thermoplastic processing, as it enables viscoplastic deformation under combined thermal (260–275 °C) and mechanical stimuli, facilitating the formation of nanoporous architectures while maintaining the material's structural integrity [29].

The self-supported C-NPMG catalyst is fabricated through a thermoplastic forming protocol that combines nanoscale pore generation and *in-situ* partial crystallization, as illustrated in Fig. 1a and Fig. S2. The as-cast MG ribbon is first heated into its SLR. In this state, due to the significantly reduced viscosity, a controlled pressure-induced deformation is applied. During this process, soluble particles are simultaneously pressed into the MG matrix. These particles act as sacrificial templates. After the thermoplastic pressing, the soluble particles are removed, leaving behind a nanoporous morphology formed through localized atomic rearrangement around the particles. Notably, the thermoplastic pressing process, which occurs at a temperature within the SLR range, also triggers *in-situ* partial crystallization. This process yields a limited quantity of nanocrystals, giving rise to a mixed-phase structure where crystalline nanodomains are dispersed within the amorphous matrix.

X-ray diffraction (XRD) analysis validates this structural evolution. The as-cast MG presents a characteristic broad diffraction halo (2θ = 30°–50°) (Fig. 1c), which is a telltale sign of

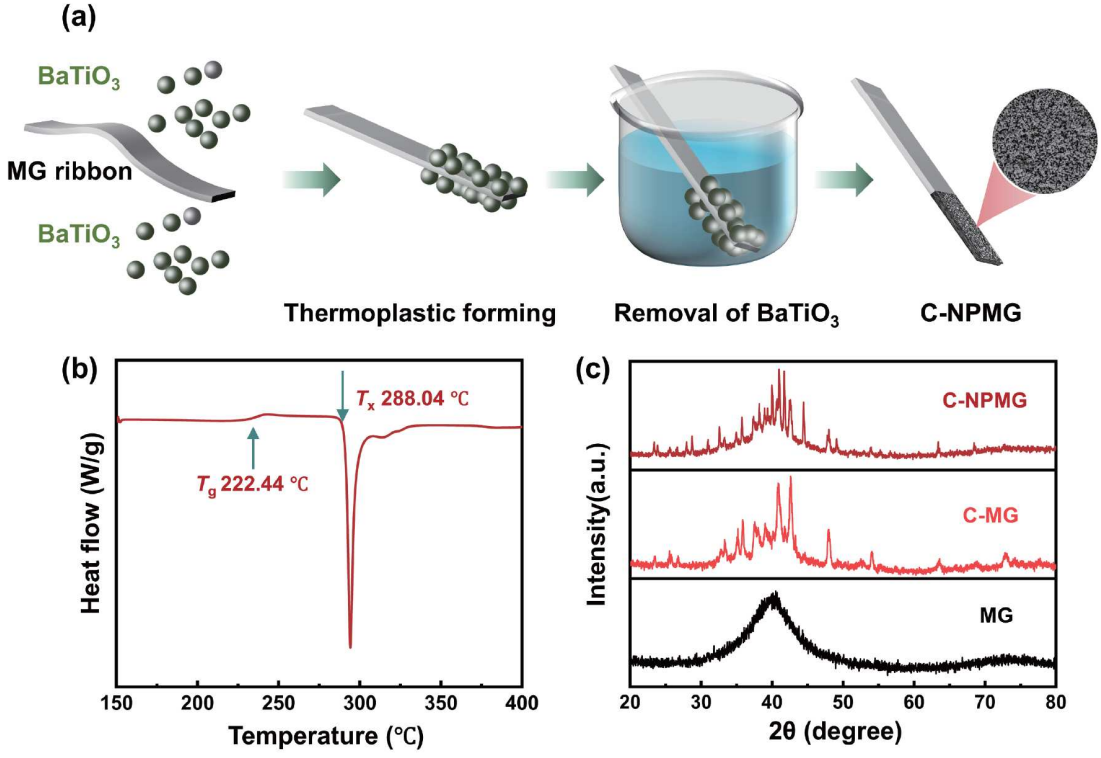

Figure 1 (a) Schematic diagram of thermoplastic forming; (b) DSC of MG thin ribbon; (c) XRD patterns of the MG, C-MG, and C-NPMG thin ribbon.

short-range atomic order but the absence of long-range periodicity. In contrast, the C-NPMG shows distinct crystalline peaks superimposed on the amorphous halo. A control sample of partially crystallized metallic glass (C-MG) prepared without the pore-forming step involving particle insertion and removal but subjected to the same temperature conditions during the thermoplastic process, shows similar crystalline peaks (Fig. 1c). However, it lacks the nanoporous structure. This comparison verifies that partial crystallization is a consequence of thermo-mechanical processing rather than compositional alterations.

Scanning electron microscopy (SEM) was employed to investigate the surface morphology of the C-NPMG electrocatalyst. The results unveiled a highly developed nanoporous structure with pore diameters spanning from 0 to 200 nm (Fig. 2a–c). These uniformly distributed pores cover nearly the entire hot-pressed surface. This nanoporous feature significantly augments the specific surface area and surface defects, thereby facilitating the exposure of more active sites, promoting reactant diffusion and electron conduction. It also plays a pivotal role in expanding the accessible interface between the electrolyte and the electrode active material, as well as enhancing mass transfer, all of which contribute to enhancing the stability and activity of the HER [30–33]. Cross-sectional SEM images of the C-NPMG thin ribbon are presented in Fig. 2d–f. Evidently, the porous portion adheres firmly to the thin ribbon, and the thickness of the porous layer is approximately 1 μm. This indicates that C-NPMG possesses a self-supporting nanoporous structure with high porosity, which further bolsters the stability and reliability of the catalyst. Compared with the coating structure, the self-supported structure reduces the charge transfer resistance at the catalyst surface [34], increasing the catalyst's charge exchange efficiency.

High-resolution transmission electron microscopy (HRTEM) images and Fourier transform (FFT) patterns of the C-NPMG, C-MG, and MG samples are illustrated in Fig. 2g–i to delve deeper into the crystalline state of the C-NPMG. Upon hot compression molding, the C-NPMG underwent a transformation from an amorphous state to a partially crystalline state. Although the majority of its regions remained in the amorphous phase, certain crystalline phase regions started to manifest. The partially crystalline composite structure effectively integrates the advantageous attributes of both the crystalline and amorphous

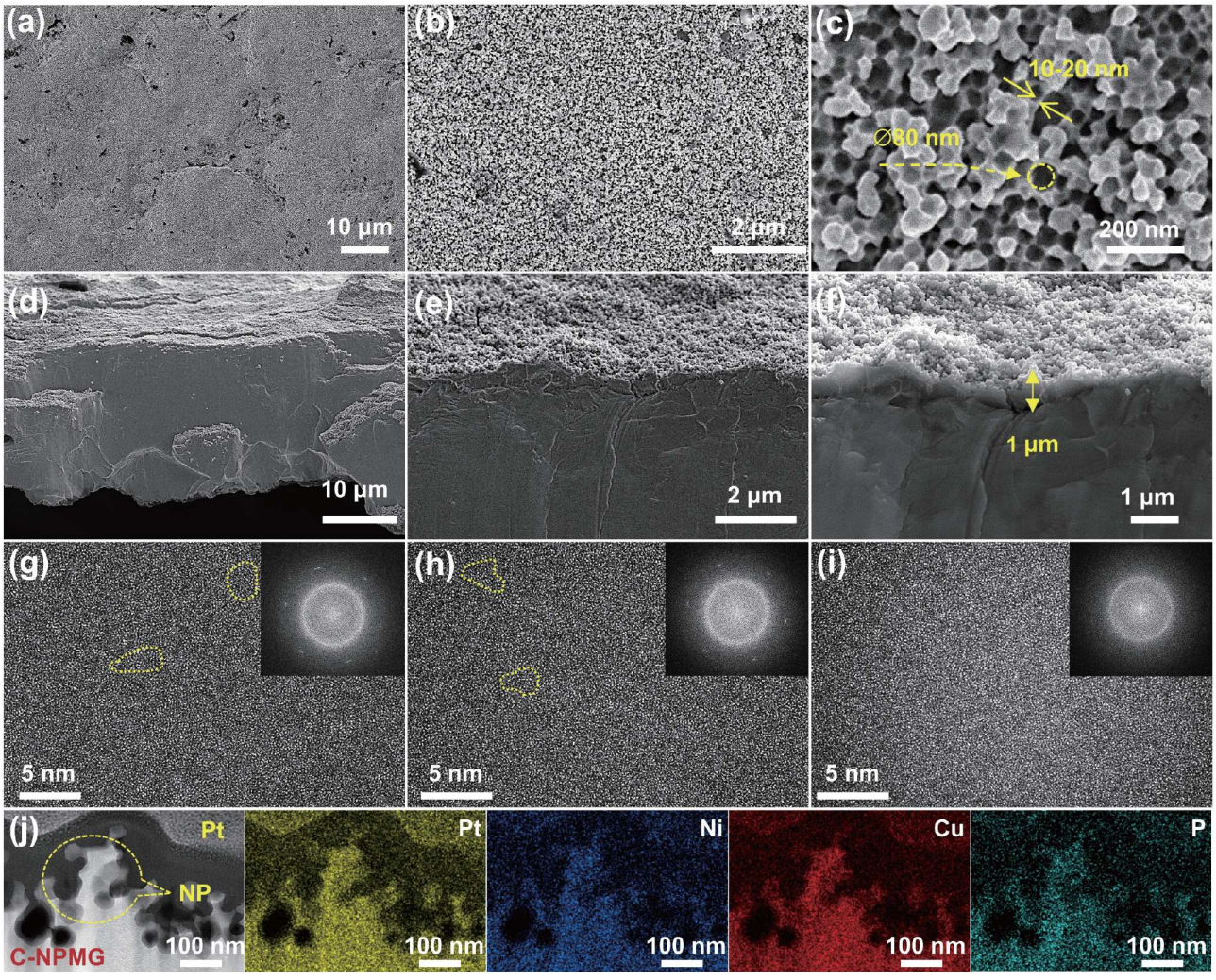

Figure 2 (a–c) SEM images of different magnifications on the surface of C-NPMG; (d–f) SEM images of different magnifications on the cross-section of C-NPMG. HRTEM and FFT images of the (g) C-NPMG, (h) C-MG, and (i) MG sample. (j) Scanning transmission electron microscopy-high angle annular dark field images of the cross-section structure of the C-NPMG sample and the corresponding EDS mapping of elements Pt, Ni, Cu, and P.

phases. It combines the high electrical conductivity inherent to the crystalline phase with the profusion of unsaturated coordination sites present in the amorphous phase. From the standpoint of electrochemical systems, within such structures, there exists a synergistic interplay between the crystalline grains and the amorphous matrix. This interplay gives rise to additional defects, thereby enhancing the catalytic activity, as documented in Reference [35]. Moreover, the abundance of phase boundaries and high kinetic energy in the partially crystalline composites augment the accessible surface area and provide more active sites, thus enabling efficient mass transfer. This structural arrangement not only elevates the bilayer capacitance but also significantly bolsters the charge transfer capabilities, as indicated in Reference [36].

In this research, the partially crystalline composite structures found in the C-MG and C-NPMG samples exhibit superior catalytic performance when juxtaposed with the purely amorphous structures of the MG samples and fully crystalline materials. This clearly underscores the pivotal role of phase boundaries and defect engineering in optimizing catalytic activity. During the crystallization process, due to the electron transfer from P to Ni, the occupation of Ni hollow sites by P, and the formation of the Ni–P bond, the charged nature of C-NPMG is analogous to that of [NiFe] hydrogenase and its analogs. This characteristic reduces the energy expenditure for H_2 desorption and substantially enhances the HER catalytic activity, as evidenced in Reference [37] and further validated by density functional theory (DFT) calculations presented in the subsequent section. These regions are replete with a large quantity of nanocrystals and possess an increased number of active sites requisite for HER catalysis, which contributes to the enhancement of the HER performance.

The MG thin ribbon was subjected to direct heat treatment, resulting in its conversion into C-MG with partial crystallization (Fig. 2h). As evidenced by the diffraction rings and HRTEM images, some nanocrystalline regions also appeared within the amorphous phase region of the C-MG. Additionally, the TEM images of the C-NPMG thin ribbon, along with the associated elemental line scanning data, are shown in Fig. S4, and the TEM images of the C-NPMG thin ribbon, together with the corresponding elemental mapping results, are presented in Fig. 2j. The uniform distribution of Pt, P, Cu, and Ni within the porous structure is clearly observable.

Electrochemical characterization

The electrocatalytic performance of the C-NPMG catalyst was comprehensively evaluated within a standard three-electrode electrochemical system. The working electrode, featuring the C-NPMG material, was immersed in three distinct electrolytes: 1.0 M KOH, 1.0 M phosphate-buffered saline (PBS), and 0.5 M H_2SO_4, all maintained at room temperature. Linear sweep voltammetry (LSV) measurements were carried out on commercial Pt plate, Pt/C (20 wt% Pt), C-NPMG, C-MG, and MG electrodes to conduct a comparative analysis. The current densities obtained were normalized to the geometric surface area of the electrodes, as depicted in Fig. 3a. Notable differences in catalytic performance were observed at a current density of 10 mA cm^{-2} (Fig. 3b). In 1.0 M KOH solution, C-NPMG exhibited exceptional catalytic activity with an overpotential (η_{10}) of 42.21 mV, outperforming both commercial Pt/C (η_{10} = 49.16 mV) and MG (η_{10} = 267.08 mV). This significant enhancement in catalytic efficiency can be attributed to the unique nanoporous structure of C-NPMG, which provides increased active surface area and improved mass transport properties.

Furthermore, the overpotential η_{10} of C-MG in the same electrolyte was determined to be 110.13 mV. Although this value is higher than the C-NPMG catalyst, it still represents a substantial improvement over the MG catalyst, whose η_{10} stands at 267.08 mV. This performance enhancement indicates that the partially crystalline composite structure of C-MG contributes to increased catalytic activity. These findings collectively demonstrate that both nanostructural engineering and crystalline phase control are effective strategies for optimizing catalytic performance in alkaline media. The distinct behavior of these catalysts underscores the importance of surface properties in optimizing catalytic efficiency for gas-evolving reactions [38].

Fig. 3c presents the Tafel plots (overpotential η versus logarithmic current density $\log|j|$) for the investigated catalysts, providing crucial insights into the HER kinetics. Tafel slope is an intrinsic property of catalysts. The C-MG catalyst demonstrates markedly improved kinetics (93.80 mV dec^{-1}) compared to the amorphous MG (214.68 mV dec^{-1}), indicating that partial crystallization substantially enhances the HER activity by modifying the electronic structure and creating favorable reaction pathways. Remarkably, the C-NPMG catalyst exhibits exceptional performance with a Tafel slope of 38.48 mV dec^{-1}, surpassing even the commercial Pt/C benchmark (42.01 mV dec^{-1}). This superior activity can be attributed to the synergistic combination of nanoporous architecture and partial crystallization. These results highlight the superior HER performance of C-NPMG and underscore the importance of structural optimization in designing efficient electrocatalysts

Specific activity (SA) represents a fundamental metric for assessing intrinsic catalytic activity, with elevated SA values directly reflecting superior catalytic performance (Fig. S5). At an overpotential of −70 mV vs. RHE, the C-NPMG catalyst achieves an exceptional SA of 0.115 mA cm^{-2}_{ECSA} (where ECSA is electrochemically active surface area), representing a 16.42-fold enhancement over commercial Pt/C (0.007 mA cm^{-2}_{ECSA}). Remarkably, when polarized to −140 mV vs. RHE, C-NPMG attains an SA of 0.596 mA cm^{-2}_{ECSA}—a 28.38-fold improvement relative to Pt/C (0.021 mA cm^{-2}_{ECSA}). These comparative analyses unambiguously demonstrate C-NPMG's exceptional intrinsic activity. Notably, while Pt/C exhibits only modest SA improvements with increasing overpotential (0.007 to 0.021 mA cm^{-2}_{ECSA}), C-NPMG shows a pronounced activity enhancement (0.115 to 0.596 mA cm^{-2}_{ECSA}). This striking contrast underscores C-NPMG's superior performance stability and exceptional catalytic efficiency under demanding high-overpotential conditions.

Electrochemical impedance spectroscopy (EIS) further probed the catalytic behavior (Fig. 3d). All EIS measured at open-circuit voltage in 1 M KOH. These parameters have been comprehensively documented both in tabulated form (Table S1). By fitting the EIS spectra of C-NPMG, C-MG, MG, and commercial Pt plate with an equivalent circuit comprising a charge-transfer resistor (R_{ct}), a series resistor (R_S), and a constant phase element (CPE), C-NPMG was found to possess the lowest series resistance (R_S) among C-NPMG, C-MG and MG samples. This indicates superior electrical conductivity, attributed to its self-supported nanoporous architecture and partially crystallized

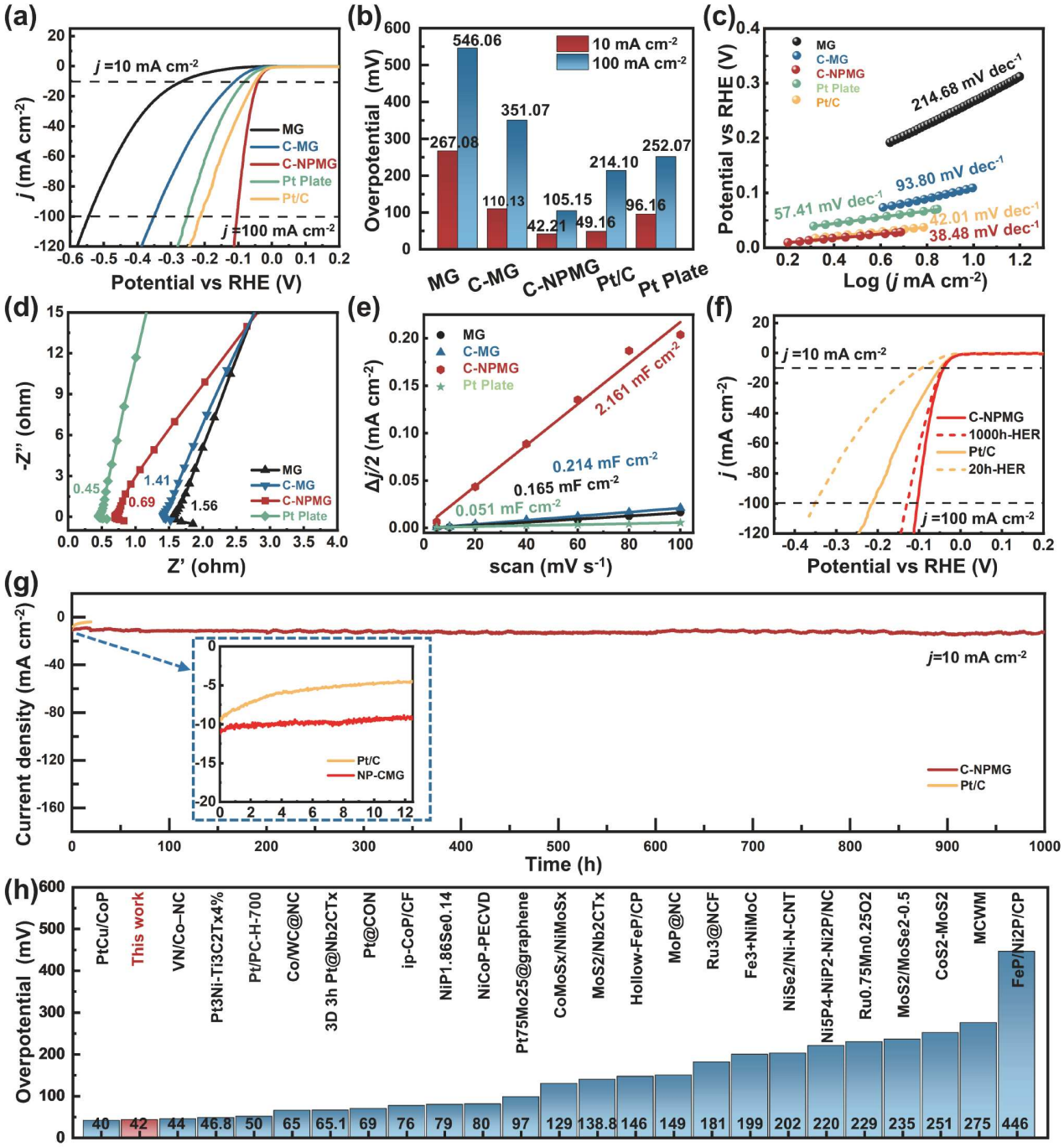

Figure 3 HER performance in 1 M KOH. (a) LSV curve compensation of MG, C-MG, C-NPMG, Pt Plate, and Pt/C at a scan rate of 2 mV s^{-1}; (b) overpotentials at 10 and 100 mA cm^{-2} of C-NPMG, C-MG, MG, Pt/C and Pt Plate; (c) corresponding Tafel plots; (d) Nyquist plots; (e) capacitive current densities against scan rates; (f) LSV curve compensation of C-NPMG and Pt/C after stability test at a scan rate of 2 mV s^{-1}; (g) stability test of the C-NPMG catalysts under a static overpotential of 10 mA cm^{-2} in 1 M KOH; (h) the comparison of the overpotential η_{10} of HER of the previous catalysts.

phase. In contrast, C-MG also showed reduced R_S compared to MG, confirming that partial crystallization promotes charge transfer.

Cyclic voltammetry (CV) was carried out in a 1 M KOH electrolyte to evaluate the ECSA of C-NPMG, MG, C-MG, and commercial Pt plates (Fig. S6). The double-layer capacitance (C_{dl}), obtained from the linear relationship between $\Delta j/2$ and the scan rate (Fig. 3e), acts as a quantitative indicator of ECSA. Remarkably, C-NPMG showed a C_{dl} of 2.161 mF cm^{-2}, significantly surpassing those of MG (0.165 mF cm^{-2}), C-MG (0.214 mF cm^{-2}), and the Pt plate (0.051 mF cm^{-2}). This represents roughly an order of magnitude increase in active sites compared to MG, highlighting the exceptional catalytic capacity of C-NPMG. The remarkable enhancement of C-NPMG's ECSA can be ascribed to its distinctive nanoporous architecture crafted via the thermoplastic processing strategy. This structural design effectively exposes a large number of active sites while preserving mechanical integrity. As a result, it optimizes both surface

reactivity and durability. The correlation between the increased ECSA and the improved catalytic performance demonstrates the effectiveness of this synthetic approach for developing high-performance electrocatalysts.

Beyond catalytic activity, operational durability is a pivotal parameter for assessing electrocatalysts in real-world applications. The cyclic voltammetry (CV) measurements were performed at the overpotential required to achieve a current density of 10 mA cm^{-2}, as annotated in Fig. 3g. The determined operating potentials were 42.21 mV vs. RHE for C-NPMG and 49.16 mV vs. RHE for the Pt/C benchmark catalyst. Commercial Pt/C catalysts are notorious for their significant performance degradation, often experiencing a 50% decline in HER activity within just 4 h of operation. In stark contrast, the C-NPMG catalyst developed in this study showcased exceptional stability during an arduous 1000-h HER test in an alkaline medium of 1 M KOH. It maintained a consistent current density of 10 mA cm^{-2} throughout the test, as illustrated in Fig. 3f–g. Notably, following this extensive testing period, the catalytic activity of C-NPMG exhibited negligible attenuation. The post-test overpotentials (η_{10} = 43.20 mV) were almost identical to the initial values (42.21 mV), as evidenced by Fig. S9. Morphological characterization, as depicted in Figs S7 and S8, further revealed the remarkable structural robustness of C-NPMG. Despite some surface restructuring during the 1000-h test, including partial dealloying and the formation of secondary nanostructures, the material largely preserved its original nanoporous architecture after undergoing acid cleaning with 1 M HCl and subsequent rinsing with deionized water. This outstanding stability can be attributed to the unique thin ribbon-stabilized, self-supporting configuration of C-NPMG [39], which effectively mitigates the agglomeration and active site loss issues commonly encountered in nanoparticle-based catalysts. The exceptional durability of C-NPMG primarily stems from its inherent amorphous characteristics. Despite partial crystallization, the metallic glass matrix maintains superior corrosion resistance [40], which plays a crucial protective role in maintaining structural stability during prolonged HER operation while providing stable catalytic active sites. The combination of its ultra-stable HER performance, with an activity loss of less than 2% after 1000 h, and excellent structural integrity firmly positions C-NPMG as a highly promising candidate for industrial water electrolysis systems. These findings far surpass the durability benchmarks established by conventional Pt/C catalysts, effectively addressing one of the major limitations in current hydrogen production technologies.

The HER performance of C-NPMG was comprehensively benchmarked against a broad spectrum of reported catalyst systems, encompassing noble metals, transition metal oxides (TMOs), dichalcogenides (TMDs), nitrides (TMNs), phosphides (TMPs), carbides (TMCs), borides (TMBs), and MG (Fig. 3h and Table S2). Comparative analysis reveals that C-NPMG exhibits superior HER activity, featuring significantly lower overpotentials in alkaline media than most catalysts within these material classes. Specifically, its η_{10} value of 42.21 mV in 1 M KOH surpasses most state-of-the-art electrocatalysts, even those containing complex nanostructures.

Importantly, C-NPMG stands out for its unique combination of exceptional catalytic activity and remarkable long-term stability, a dual advantage rarely achieved by existing HER catalysts (Fig. S10 and Table S3). While many high-activity catalysts suffer from rapid degradation, and stable catalysts often lack sufficient reactivity, C-NPMG maintains <2% activity loss after 1000 h of continuous operation, a performance unattained by conventional Pt-based and non-noble metal catalysts. This superior profile—characterized by low overpotential, high conductivity, and structural robustness—positions C-NPMG as a transformative candidate for practical hydrogen production.

In a neutral 1 M PBS electrolyte, the C-NPMG catalyst demonstrated superior HER performance over the amorphous MG and commercial Pt-based catalysts. As illustrated in Fig. 4a–d, C-NPMG exhibited a significantly reduced HER overpotential (η_{10} = 88.03 mV), starkly lower than the values observed for MG (206.38 mV) and the Pt plate (188.52 mV). While the Pt/C catalyst displayed favorable initial activity at low current densities (η_{10} = 44.58 mV), its performance deteriorated substantially under higher current demands, indicative of poor stability in rigorous operational conditions. In contrast, C-NPMG maintained exceptional catalytic activity even at elevated current densities, showcasing robust and sustained hydrogen production capabilities. This superior high-current performance highlights C-NPMG's pronounced advantage in stability and efficiency compared to Pt/C, positioning it as a viable candidate for large-scale hydrogen generation. Kinetic analysis via Tafel plots revealed that C-NPMG possessed a Tafel slope of 79.19 mV dec^{-1} in PBS, significantly lower than that of the MG (174.55 mV dec^{-1}, Fig. 4c). This reduction in the Tafel slope signifies a faster reaction kinetics, likely enabled by the catalyst's nanoporous structure and crystalline-amorphous interfacial sites, facilitating efficient electron transfer and hydrogen adsorption/desorption.

Consistent with the alkaline environment results, EIS was employed to characterize the catalytic behavior in neutral media (Fig. S11). All EIS measurements were conducted at open-circuit potential in 1 M PBS solution. Equivalent circuit modeling of the EIS spectra (incorporating charge-transfer resistance (R_{ct}), R_S, and constant phase element (CPE)) revealed that C-NPMG exhibited the lowest series resistance (R_S = 3.49 Ω) among the tested samples (C-MG and MG). This minimal R_S value indicates superior electrical conductivity, which we attribute to the material's unique combination of self-supported nanoporous architecture and partially crystalline phase. CV measurements (Fig. S12) further quantified the ECSA, revealing that C-NPMG harbored approximately sevenfold more active sites than MG. This was corroborated by its significantly higher double-layer capacitance (C_{dl} = 0.932 mF cm^{-2}) compared to MG (0.122 mF cm^{-2}, Fig. 4d), directly linking its nanostructural design to enhanced surface reactivity in neutral media.

Beyond catalytic activity, operational durability represents a critical performance metric for practical electrocatalyst applications. The determined operating potentials were 88.03 mV vs. RHE for C-NPMG and 44.58 mV vs. RHE for the Pt/C benchmark catalyst. Commercial Pt/C catalysts exhibit substantial performance degradation, typically showing a 50% decrease in hydrogen evolution reaction (HER) activity within merely 9 h of operation, with continued deterioration over time (Fig. S13). In striking contrast, our developed C-NPMG catalyst demonstrates exceptional stability under demanding HER conditions (1 M PBS, 100 h operation at 10 mA cm^{-2}). The initial performance fluctuations observed during the first 10 h (Fig. S13) likely result from beneficial surface reconstruction and active site optimization processes. Remarkably, the catalyst subsequently achieves

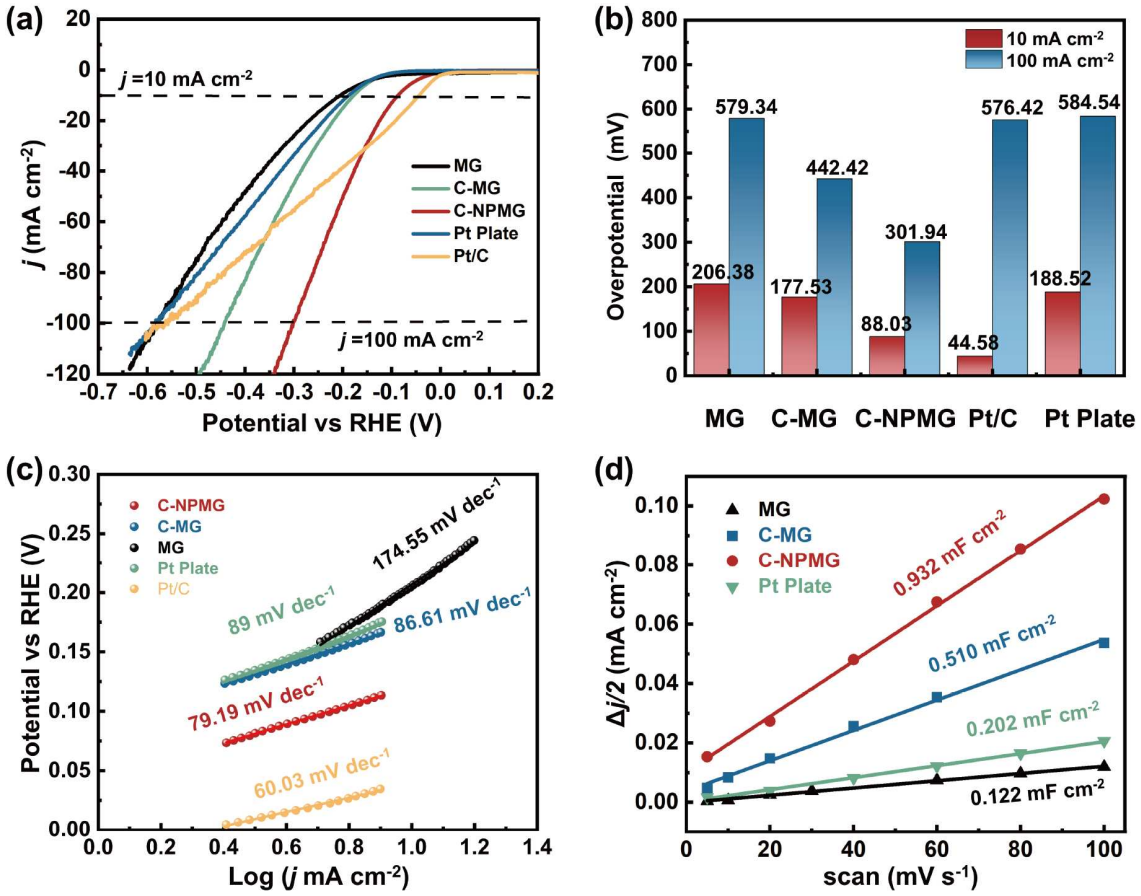

Figure 4 HER performance in 1 M PBS. (a) LSV curve compensation of MG, C-MG, C-NPMG, Pt Plate, and Pt/C at a scan rate of 2 mV s^{-1}; (b) overpotentials at 10 and 100 mA cm^{-2} of C-NPMG, C-MG, MG, Pt/C and Pt plate; (c) corresponding Tafel plots; (d) capacitive current densities against scan rates.

outstanding stability, maintaining consistent current density throughout the remaining 90-h test period. These results clearly demonstrate that C-NPMG exhibits excellent HER stability even in neutral environments.

In 0.5 M H_2SO_4, the C-NPMG catalyst demonstrated exceptional HER activity, outperforming both MG and commercial Pt-based catalysts across a wide current density range. As shown in Fig. 5a–d, at the low current density of 10 mA cm^{-2}, C-NPMG achieved an overpotential (η_{10} = 18.01 mV)—slightly superior to Pt/C (21.34 mV) and far lower than MG (176.98 mV) and the Pt plate (49.08 mV). Notably, under high current densities (100 mA cm^{-2}), a critical metric for large-scale electrolysis, C-NPMG exhibited a pronounced performance edge with an overpotential (η_{100} = 87.05 mV)—substantially lower than Pt/C (124.22 mV). While Pt/C catalysts often suffer from increased overpotential and stability issues at high currents due to particle agglomeration and corrosion, C-NPMG maintained its structural integrity and active site accessibility, enabling efficient HER even under demanding conditions. This disparity in high-current performance underscores the superiority of C-NPMG's nanoporous, partially crystalline architecture, which minimizes mass transport resistance and enhances charge transfer kinetics. Kinetic analysis via Tafel plots revealed a Tafel slope of 42.87 mV dec^{-1} for C-NPMG (Fig. 5c), significantly lower than MG (115.86 mV dec^{-1}), indicating rapid charge-transfer kinetics and favorable hydrogen adsorption/desorption behavior.

Consistent with the observations in alkaline and neutral environments, EIS was utilized to investigate the catalytic performance in acidic media (0.5 M H_2SO_4, Fig. S14). All EIS measurements were performed at open-circuit potential. Equivalent circuit analysis (comprising R_{ct}, R_S, and a CPE) revealed that C-NPMG exhibited the lowest R_S (0.619 Ω) among the tested samples (C-MG and MG). This minimal resistance underscores the material's superior electrical conductivity, which originates from its unique self-supported nanoporous framework and partially crystalline structure. CV measurements (Fig. S15) further confirmed that C-NPMG possessed an ECSA approximately eight times larger than MG, supported by its higher double-layer capacitance (C_{dl} = 0.478 mF cm^{-2} vs. 0.057 mF cm^{-2} for MG; Fig. 5d). This combination of abundant active sites and robust structural stability allows C-NPMG to excel at low currents and outperform Pt-based catalysts at the high current densities required for industrial water splitting.

Beyond catalytic activity, operational durability serves as a crucial performance metric for evaluating electrocatalysts in practical applications. The determined operating potentials were 18.01 mV vs. RHE for C-NPMG and 21.34 mV vs. RHE for the Pt/C benchmark catalyst. Commercial Pt/C catalysts suffer from rapid performance degradation, exhibiting a 25% decline in HER activity within merely 9 h of operation, with continued deterioration observed over extended periods (Fig. S16). In marked

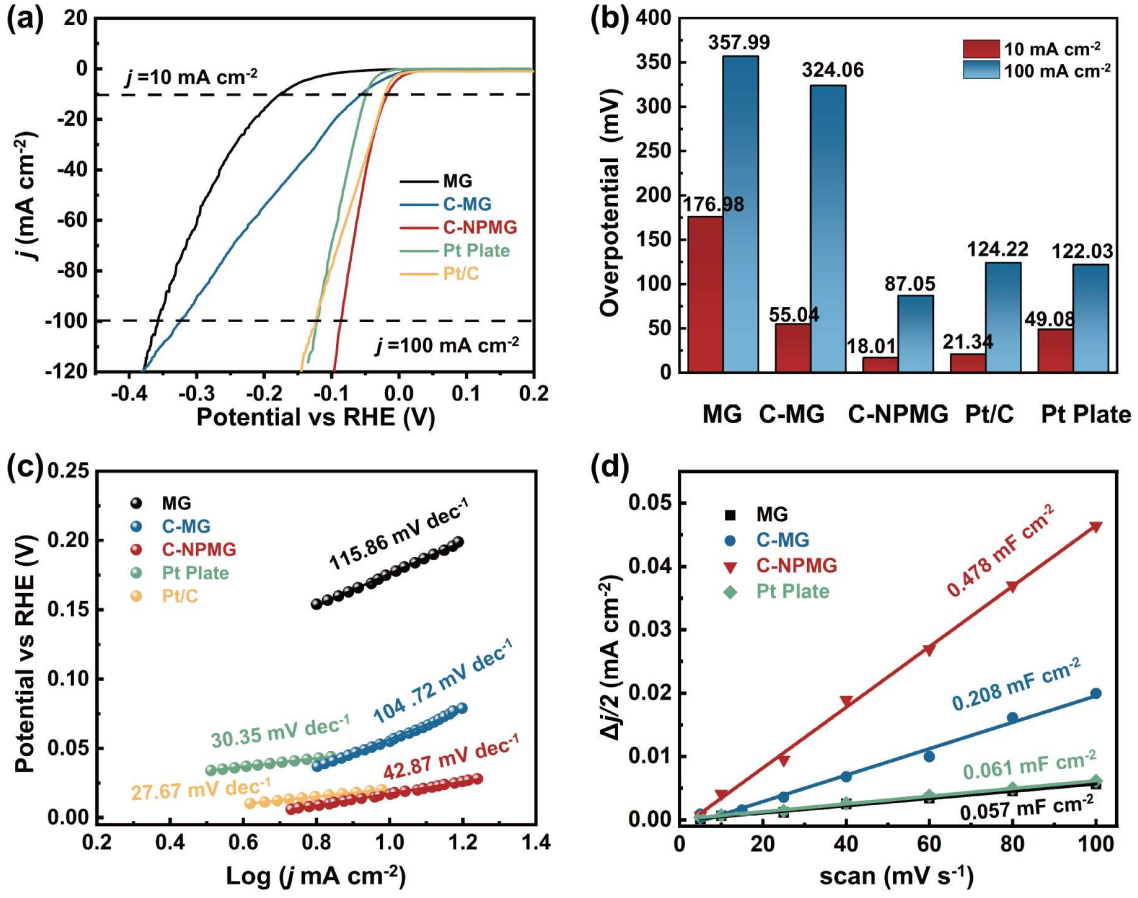

Figure 5 HER performance in 0.5 M H_2SO_4. (a) LSV curve compensation of MG, C-MG, C-NPMG, Pt plate, and Pt/C at a scan rate of 2 mV s^{-1}; (b) overpotentials at 10 and 100 mA cm^{-2} of MG, C-MG, C-NPMG, Pt plate, and Pt/C; (c) corresponding Tafel plots; (d) capacitive current densities against scan rates.

contrast, our C-NPMG catalyst demonstrates exceptional stability under demanding HER conditions (0.5 M H_2SO_4, 100 h continuous operation at 10 mA cm^{-2}). The initial performance variations during the first 6 h (Fig. S16) are likely associated with beneficial surface reconstruction and active site optimization processes. Following this activation period, the catalyst maintains outstanding stability, showing negligible current density variation throughout the subsequent 94 h of continuous operation. These results unequivocally demonstrate that C-NPMG exhibits superior HER stability even under highly acidic conditions.

C-NPMG maintained robust HER performance across acidic, neutral, and alkaline electrolytes (Figs 3–5), suggesting that its nanoporous architecture facilitates efficient proton adsorption and hydrogen desorption regardless of pH. The comparative data further demonstrate that C-NPMG outperforms benchmark catalysts across diverse material families in alkaline conditions and shows promise in neutral and acidic electrolytes (Tables S4 and S5). By integrating nanoporous architecture, partial crystallization, and a self-supported design, this work establishes a new paradigm for electrocatalyst engineering, where synergistic structural features enable breakthroughs in both activity and durability. These findings highlight C-NPMG's potential to overcome the trade-offs between performance and stability in electrochemical water splitting, paving the way for its translation to industrial-scale hydrogen generation technologies.

Elemental changes after long-term stability test

X-ray photoelectron spectroscopy (XPS) was utilized to explore the elemental composition and valence state alterations of the catalysts under diverse conditions. Three representative samples (MG, C-NPMG, and C-NPMG) were examined after long-term HER (After-HER). The Pt 4f spectra (Fig. S17a) revealed subtle changes in the platinum chemical environment, emphasizing minimal alterations despite prolonged electrochemical operation. After extended HER operation, C-NPMG showed a slight rise in the Pt^{2+} peak intensity, along with a positive shift in the Pt^{2+} binding energies and a corresponding negative shift in the Pt^0 peaks. Nevertheless, the overall valence state distribution remained largely unaltered, highlighting the remarkable stability of platinum during the long-term HER process.

The Ni 2f speciation analysis (Fig. S17b) presented distinct evolution trends. Compared with the MG reference, the Ni^0 peak in C-NPMG had a minor negative shift. After long-term HER testing, a significant decrease in the Ni^0 surface concentration was observed, accompanied by a concurrent increase in the Ni^{2+} signal intensity. This indicates progressive surface oxidation during electrocatalysis.

The Cu 2f characterization (Fig. S17c) revealed notable changes. Both Cu^0 and Cu^{2+} peaks exhibited negative binding energy shifts and significant attenuation after HER operation, suggesting the surface depletion of copper species.

The P analysis (Fig. S17d) demonstrated substantial signal

attenuation after HER, with C-NPMG showing a slightly less pronounced reduction. This behavior implies that surface P atoms in the nanoporous structure have weaker interatomic coordination than the bulk regions, making them more vulnerable to removal during prolonged electrochemical operation.

XPS spectral analysis reveals that there is significant electron transfer from phosphorus to nickel during crystallization in C-NPMG. This results in a slightly positive charge on Ni (δ^+) and a corresponding negative charge on P (δ^-), a configuration highly similar to the active sites of [NiFe] hydrogenases and their synthetic analogs [41], which are renowned for their outstanding HER activity. The catalytic enhancement mechanism involves P atoms occupying Ni hollow sites, effectively lowering the energy barrier for hydrogen desorption. This unique electronic structure significantly contributes to the material's excellent HER performance.

XPS analysis after HER reveals that Pt primarily exists in the metallic state, although it undergoes partial surface oxidation, while copper, nickel, and phosphorus exhibit significant oxidation and dissolution. This selective dissolution leads to the enrichment of platinum on the catalyst surface and the continuous regeneration of fresh active sites. Such a self-reconstruction process helps maintain high catalytic activity during long-term operation [42]. Furthermore, this selective dissolution can increase defect density, thereby enhancing the intrinsic activity of the catalyst, enriching active sites, and improving conductivity, which is more favorable for HER [43]. This self-optimization approach is similar to the idea proposed by Jeon *et al.* [44] that an increase in the Pt concentration on the surface of Pt-M alloys moves the d-band center (ε_d) to a higher electronic energy level (closer to the Fermi level, E_F), which improves the catalytic activity of the material similarly. Consequently, this dynamic surface reconstruction not only preserves the initial catalytic functionality but also progressively enhances catalytic efficiency over time.

Porous nanostructures and microstructures to improve HER

The catalytic efficiency of nanoporous catalysts can be significantly optimized by tailoring surface wettability to enhance reactant accessibility and gas release kinetics [45–49]. To uncover the structural origins of C-NPMG's superior HER performance, contact angle measurements were conducted to characterize the wetting properties of C-NPMG, C-MG, and MG. As shown in Fig. 6a–c, the water contact angles (WCAs) of these catalysts in air were 7° ± 1° for C-NPMG, 70° ± 0.5° for C-MG, and 79° ± 2° for MG. These results demonstrate that C-NPMG's unique architecture, comprising TEM-confirmed nanocrystalline domains and interconnected nanoporosity, synergistically enhances surface hydrophilicity. This extreme hydrophilicity (WCA ≈ 7°) enables rapid water penetration into the porous matrix, a feature critical for optimizing HER kinetics by ensuring efficient electrolyte-catalyst contact [50].

Complementary bubble contact angle (BCA) measurements in aqueous media (Fig. 6d–f) revealed a striking contrast: C-NPMG exhibited a BCA of 144° ± 1°, significantly higher than C-MG (123° ± 1°) and MG (113° ± 1°). The elevated BCA of C-NPMG indicates superior gas-phobic behavior, attributed to its hierarchical nanostructure that minimizes bubble adhesion. This property prevents active site blockage by hydrogen bubbles, thereby maintaining continuous electrolyte access during catalysis and providing a key advantage over smooth or less porous counterparts [51–53].

The hyperhydrophilic surface of C-NPMG was further validated by ultrafast water droplet submersion, with complete wetting achieved in less than 0.75 s (Fig. 6g). Its gas-phobicity ensured stable bubble detachment at a consistent BCA of 144° ± 1° (Fig. 6h). During HER, these dual properties—extreme hydrophilicity for efficient water adsorption and robust gas-phobicity for rapid bubble release—create a highly favorable reaction microenvironment. The nanoporous surface increases the effective electrochemically active area by promoting intimate electrolyte contact, while the rough nanostructure reduces bubble adhesion forces, enabling quick detachment of small hydrogen bubbles (Fig. 6i). In contrast, the smooth MG surface suffers from strong bubble pinning, leading to active site passivation and reduced reaction efficiency.

This structural design, integrating hydrophilic nanoporosity with gas-repellent features, endows C-NPMG with two critical advantages. First, ultra-wetting properties enhance the mass transport of water molecules to catalytic sites. Second, low-adhesion bubble release ensures unimpeded gas evolution. Together, these properties mitigate kinetic limitations and prevent surface fouling, explaining the catalyst's exceptional performance across all electrolyte conditions. The synergy between nanostructured wettability and electrochemical activity highlights the importance of multiscale architecture in designing electrocatalysts for efficient hydrogen production.

DFT calculations

The Gibbs free energy of hydrogen adsorption (ΔG_{H^*}) serves as a pivotal descriptor for evaluating electrocatalytic HER activity, with values approaching zero indicating optimal adsorption/desorption kinetics [54,55]. To elucidate the impact of partial crystallization on hydrogen adsorption energetics, first-principles calculations based on DFT were performed for both partially crystalline C-MG and amorphous pure MG.

As shown in Fig. S18a, the calculated ΔG_{H^*} values were 0.302 eV for C-MG and 0.589 eV for pure MG, revealing that partial crystallization reduces the absolute value of ΔG_{H^*} by 0.287 eV, bringing it closer to the ideal thermodynamic window for efficient HER. This shift indicates that the partially crystalline structure optimizes hydrogen binding strength, balancing adsorption favorability and desorption ease to enhance catalytic kinetics.

The optimized H* adsorption configuration on the C-MG surface (Fig. S18b) highlights a unique charge density distribution that promotes efficient hydrogen intermediate interactions. Differential charge density analysis confirms strong electron transfer from adsorbed H* to adjacent Pd atoms, facilitated by the Pt-Pd alloyed active sites in the crystalline domains. This electronic redistribution weakens H–H bonding and lowers the energy barrier for hydrogen desorption, a critical step in overcoming kinetic limitations during HER [56].

The superior performance of C-MG originates from its hybrid crystalline-amorphous architecture (Fig. S18c, d), where nanocrystalline phases provide high electrical conductivity and well-defined active sites, while the amorphous matrix offers abundant unsaturated coordination environments. This synergy creates a dual-function surface: the crystalline regions enable rapid charge transfer, and the amorphous regions increase active site density through structural disorder. DFT calculations thus confirm that

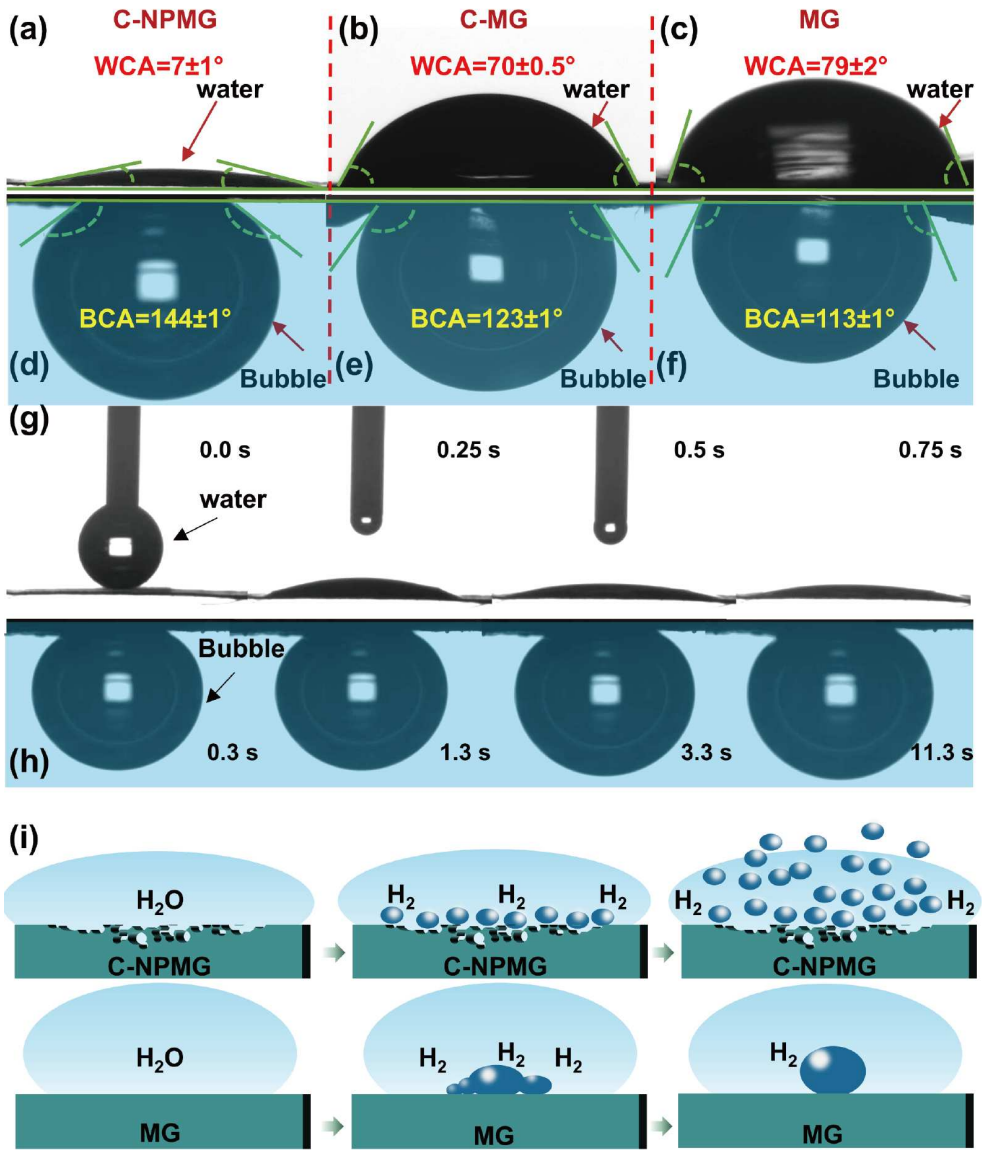

Figure 6 Water droplet contact angles of (a) C-NPMG, (b) C-MG, (c) MG; bubble contact angle of (d) C-NPMG, (e) C-MG, (f) MG; (g) the evolution of water drops on C-NPMG at the initial stage; (h) the evolution of a bubble on C-NPMG at the initial stage; (i) hydrogen escape schematic on the surface of the C-NPMG and MG.

partial crystallization not only modulates the electronic structure of metallic sites but also optimizes the hydrogen adsorption energy landscape, collectively driving the enhanced HER activity observed in experimental measurements. These theoretical insights underscore the importance of rational structural design at the atomic scale to achieve breakthroughs in electrocatalyst efficiency.

CONCLUSIONS

We report a scalable strategy to fabricate C-NPMG, a nanoporous thin-ribbon catalyst with exceptional HER performance across acidic, neutral, and alkaline electrolytes. At 10 mA cm^{-2}, it achieves ultralow overpotentials (18.01 mV in acid, 42.21 mV in alkali, 88.03 mV in neutral) and maintains < 2% activity loss after 1000 h, outperforming state-of-the-art Pt-based catalysts in durability and pH universality.

C-NPMG's superiority stems from its synergistic architecture: a self-supported nanoporous structure boosts ECSA and mass transport, while partial crystallization optimizes hydrogen adsorption energy (DFT-confirmed ΔG_{H^*} reduction) for fast kinetics. Its hierarchical nanostructure enables extreme hydrophilicity (7° water contact angle) for efficient electrolyte access and gas-phobicity (144° bubble contact angle) to prevent bubble blockage, critical for high-current stability (e.g., η_{100} = 87 mV in acid). XPS reveals dynamic surface evolution—selective dissolution of Ni/Cu/P forms a Pt-enriched layer, sustaining active sites over time.

This work establishes a new design paradigm by integrating nanoscale porosity, crystalline-amorphous synergy, and self-supported mechanics, overcoming the trade-off between activity and stability. The scalable fabrication method offers a cost-effective path for industrial hydrogen production, positioning C-NPMG as a transformative catalyst for efficient, durable water splitting across diverse technologies.

Received 29 April 2025; accepted 20 June 2025; published online 4 January 2026

1 Shi Q, Zhu C, Du D, *et al.* Robust noble metal-based electrocatalysts for oxygen evolution reaction. Chem Soc Rev, 2019, 48: 3181–3192
2 You B, Sun Y. Innovative strategies for electrocatalytic water splitting. Acc Chem Res, 2018, 51: 1571–1580
3 Koo KY, Im HB, Song D, *et al.* Ammonia decomposition over Ru-coated metal-structured catalysts for CO_x-free hydrogen production. Int J Hydrogen Energy, 2024, 52: 534–545
4 Yan Y, Xia BY, Zhao B, *et al.* A review on noble-metal-free bifunctional heterogeneous catalysts for overall electrochemical water splitting. J Mater Chem A, 2016, 4: 17587–17603
5 Yu F, Yu L, Mishra IK, *et al.* Recent developments in earth-abundant and non-noble electrocatalysts for water electrolysis. Mater Today Phys, 2018, 7: 121–138
6 Zhang J, Wang X. Solar water splitting at λ = 600 nm: a step closer to sustainable hydrogen production. Angew Chem Int Ed, 2015, 54: 7230–7232
7 Li L, Yu D, Li P, *et al.* Interfacial electronic coupling of ultrathin transition-metal hydroxide nanosheets with layered MXenes as a new prototype for platinum-like hydrogen evolution. Energy Environ Sci, 2021, 14: 6419–6427
8 Strmcnik D, Uchimura M, Wang C, *et al.* Improving the hydrogen oxidation reaction rate by promotion of hydroxyl adsorption. Nat Chem, 2013, 5: 300–306
9 Ullah F, Gilani MA, Imran M, *et al.* Potential of first row transition metal decorated graphtriyne quantum dots as single atom catalysts towards hydrogen evolution reaction (HER). Phys Scr, 2023, 98: 115308
10 Jiang B, Cui Y, Shi S, *et al.* Preparation of highly active transition bimetallic nitride nimon hydrogen evolution reaction (HER) catalyst and its performance study in seawater electrolysis. Acta Chim Sin, 2022, 80: 1394–1400
11 Jiao S, Fu X, Wang S, *et al.* Perfecting electrocatalysts via imperfections: towards the large-scale deployment of water electrolysis technology. Energy Environ Sci, 2021, 14: 1722–1770
12 Hu C, Zhang L, Gong J. Recent progress made in the mechanism comprehension and design of electrocatalysts for alkaline water splitting. Energy Environ Sci, 2019, 12: 2620–2645
13 Li B, Cao R, Zhu H, *et al.* Theoretical study of electrochemical hydrogen evolution reaction of Pt–Co diatomic sites catalyst. Int J Hydrogen Energy, 2024, 68: 559–565
14 Hu YC, Sun CX, Sun CW. Functional applications of metallic glasses in electrocatalysis. ChemCatChem, 2019, 11: 2401–2414
15 Tian J, Hu Y, Lu W, *et al.* Dealloying of an amorphous TiCuRu alloy results in a nanostructured electrocatalyst for hydrogen evolution reaction. Carbon Energy, 2023, 5: e322
16 Ruan W, Zhang H, Fu J, *et al.* Dissolution manufacturing strategy for designing efficient and low cost polymeric solar water evaporator. Adv Funct Mater, 2024, 34: 2312314
17 Liu D, Song Z, Cheng S, *et al.* Mesoporous IrNiTa metal glass ribbon as a superior self-standing bifunctional catalyst for water electrolysis. Chem Eng J, 2022, 431: 134210
18 Chai YM, Shang X, Gao WK, *et al.* Liquid crystal template assisted electrodeposition of molybdenum sulfide nanoparticles supported on carbon fiber as efficient electrocatalyst for hydrogen evolution reaction. Int J Electrochem Sci, 2018, 13: 5488–5496
19 Liu Y, Liu J, Sohn S, *et al.* Metallic glass nanostructures of tunable shape and composition. Nat Commun, 2015, 6: 7043
20 Zeeshan MA, Esqué-de los Ojos D, Castro-Hartmann P, *et al.* Electrochemically synthesized amorphous and crystalline nanowires: dissimilar nanomechanical behavior in comparison with homologous flat films. Nanoscale, 2016, 8: 1344–1351
21 Wang WH. Bulk metallic glasses with functional physical properties. Adv Mater, 2009, 21: 4524–4544
22 Chen M. A brief overview of bulk metallic glasses. NPG Asia Mater, 2011, 3: 82–90
23 Ma J, Huang Z, Zheng H, *et al.* Controllable thermoplastic forming of bulk metallic glasses in milliseconds by resistance welding forming. Mater Res Express, 2019, 6: 075210
24 Fu J, Li Z, Liu Z, *et al.* Manufacture of porous metallic glass using dissolvable templates. Sci China Mater, 2022, 65: 2833–2841
25 Sun Y, He H, Zheng D, *et al.* Facile synthesis of ultrafine $RuTe_2$ nanoparticles supported on B,N co-doped graphene as an efficient HER catalyst. Int J Hydrogen Energy, 2024, 49: 955–963
26 Yang H, Chen Z, Guo P, *et al.* B-doping-induced amorphization of LDH for large-current-density hydrogen evolution reaction. Appl Catal B-Environ, 2020, 261: 118240
27 Yan Y, Wang C, Huang Z, *et al.* Highly efficient and robust catalysts for the hydrogen evolution reaction by surface nano engineering of metallic glass. J Mater Chem A, 2021, 9: 5415–5424
28 Nagase T, Hosokawa T, Umakoshi Y. Temperature dependence of MeV-electron-irradiation-induced nanocrystallization in Zr-Pt metallic glass. Intermetallics, 2010, 18: 767–772
29 Li X, Liang X, Zhang Z, *et al.* Cold joining to fabricate large size metallic glasses by the ultrasonic vibrations. Scripta Mater, 2020, 185: 100–104
30 Zhao F, Liu H, Zhu H, *et al.* Amorphous/amorphous Ni-P/$Ni(OH)_2$ heterostructure nanotubes for an efficient alkaline hydrogen evolution reaction. J Mater Chem A, 2021, 9: 10169–10179
31 Jin D, Yu A, Lee Y, *et al.* Ni_xRh_{1-x} bimetallic alloy nanofibers as a pH-universal electrocatalyst for the hydrogen evolution reaction: the synthetic strategy and fascinating electroactivity. J Mater Chem A, 2020, 8: 8629–8637
32 Liu P, Wang J, Sui Y, *et al.* Nanosurface-induced construction of NiCoP-CoP heterostructure nanobristle electrodes for highly efficient alkaline hydrogen evolution reaction. J Mater Chem A, 2023, 11: 22340–22346
33 Bartoli F, Capozzoli L, Peruzzolo T, *et al.* Probing the activity and stability of MoO_2 surface nanorod arrays for hydrogen evolution in an anion exchange membrane multi-cell water electrolysis stack. J Mater Chem A, 2023, 11: 5789–5800
34 Lukowski MA, Daniel AS, Meng F, *et al.* Enhanced hydrogen evolution catalysis from chemically exfoliated metallic MoS_2 nanosheets. J Am Chem Soc, 2013, 135: 10274–10277
35 Wang PP, Wang JQ, Huo JT, *et al.* Fast degradation of azo dye by nanocrystallized Fe-based alloys. Sci China-Phys Mech Astron, 2017, 60: 076112
36 Li D, Qin Y, Liu J, *et al.* Dense crystalline-amorphous interfacial sites for enhanced electrocatalytic oxygen evolution. Adv Funct Mater, 2022, 32: 2107056
37 Chen Y, Zhang J, Wan L, *et al.* Effect of nickel phosphide nanoparticles crystallization on hydrogen evolution reaction catalytic performance. Trans Nonferrous Met Soc China, 2017, 27: 369–376
38 Zeng S, Ruan W, Chen Z, *et al.* Dissolution manufacturing strategy for the facile synthesis of nanoporous metallic glass multifunctional catalyst. Small Methods, 2025, 9: 2401109
39 Li J, Wen Z, Hui ZX, *et al.* Graphene-MoS_2 vertically anchored on an MXene-derived accordion-like TiO_2/C skeleton: an ultrastable HER catalyst. J Mater Chem A, 2020, 8: 14223–14233
40 Yang X, Gao M, Liu Y, *et al.* Superior corrosion resistance of high-temperature Ir–Ni–Ta–(B) amorphous alloy in sulfuric acid solution. Corrosion Sci, 2022, 200: 110227
41 Léger C, Dementin S, Bertrand P, *et al.* Inhibition and aerobic inactivation kinetics of *Desulfovibrio fructosovorans* NiFe hydrogenase studied by protein film voltammetry. J Am Chem Soc, 2004, 126: 12162–12172
42 Doubek G, Sekol RC, Li J, *et al.* Guided evolution of bulk metallic glass nanostructures: a platform for designing 3D electrocatalytic surfaces. Adv Mater, 2016, 28: 1940–1949
43 Zhang Y, Pan J, Gong G, *et al. In situ* surface reconstruction of catalysts for enhanced hydrogen evolution. Catalysts, 2023, 13: 120
44 Jeon TY, Kim SK, Pinna N, *et al.* Selective dissolution of surface nickel close to platinum in PTNI nanocatalyst toward oxygen reduction reaction. Chem Mater, 2016, 28: 1879–1887
45 Chandrasekaran S, Kim EJ, Chung JS, *et al.* High performance bifunctional electrocatalytic activity of a reduced graphene oxide–molybdenum oxide hybrid catalyst. J Mater Chem A, 2016, 4: 13271–

13279
46 Nishimura S, Ebitani K. Recent advances in heterogeneous catalysis with controlled nanostructured precious monometals. ChemCatChem, 2016, 8: 2303–2316
47 Chandrasekaran S, Yao L, Deng L, *et al.* Recent advances in metal sulfides: from controlled fabrication to electrocatalytic, photocatalytic and photoelectrochemical water splitting and beyond. Chem Soc Rev, 2019, 48: 4178–4280
48 Chandrasekaran S, Khandelwal M, Dayong F, *et al.* Developments and perspectives on robust nano- and microstructured binder-free electrodes for bifunctional water electrolysis and beyond. Adv Energy Mater, 2022, 12: 2200409
49 Ahsan MA, He T, Eid K, *et al.* Controlling the interfacial charge polarization of mof-derived 0D–2D vdW architectures as a unique strategy for bifunctional oxygen electrocatalysis. ACS Appl Mater Interfaces, 2022, 14: 3919–3929
50 Zhang H, Fornell J, Feng Y, *et al.* Inducing surface nanoporosity on Fe-based metallic glass matrix composites by selective dealloying. Mater Charact, 2019, 153: 46–51
51 Cheng W, Zhao X, Su H, *et al.* Lattice-strained metal-organic-framework arrays for bifunctional oxygen electrocatalysis. Nat Energy, 2019, 4: 115–122
52 Niu S, Jiang WJ, Tang T, *et al.* Autogenous growth of hierarchical NiFe $(OH)_x$/FeS nanosheet-on-microsheet arrays for synergistically enhanced high-output water oxidation. Adv Funct Mater, 2019, 29: 1902180
53 Zhao X, Ren H, Luo L. Gas bubbles in electrochemical gas evolution reactions. Langmuir, 2019, 35: 5392–5408
54 Yang C, Zhao R, Xiang H, *et al.* Ni-activated transition metal carbides for efficient hydrogen evolution in acidic and alkaline solutions. Adv Energy Mater, 2020, 10: 2002260
55 Liu S, Zhang Z, Dastafkan K, *et al.* Yttrium-doped NiMo-MoO_2 heterostructure electrocatalysts for hydrogen production from alkaline seawater. Nat Commun, 2025, 16: 773
56 Hu YC, Wang YZ, Su R, *et al.* A highly efficient and self-stabilizing metallic-glass catalyst for electrochemical hydrogen generation. Adv Mater, 2016, 28: 10293–10297

Acknowledgement This work was financially supported by the Key-Area Research and Development Program of Guangdong Province (2024B0101070001), the National Natural Science Foundation of China (52401217, 52201186, 52371160, 52271150, and 52201185), the Applied Research Program of Guangdong Province (2019B030302010), and the Science and Technology Innovation Commission of Shenzhen (RCJC20221008092730037 and 20220804091920001). We thank the Instrumental Analysis Center of Shenzhen University for the assistance with the electron microscope.

Author contributions Jiang J wrote the manuscript, created visualizations, developed the methodology, conducted the investigation, and curated the data. Zeng S performed formal analysis and assisted in the investigation. Lin J was involved in the investigation and conceptualization. Zhao X participated in the investigation. Fu J reviewed and edited the manuscript, and contributed to the methodology and data curation. Liu X supervised the research, provided resources, and helped develop the methodology. Chen Q contributed to the methodology and formal analysis. Ruan W reviewed and edited the manuscript, curated data, supervised the project, and contributed to the study's conceptualization. Ma J reviewed and edited the manuscript, created visualizations, supervised the project, provided resources, and contributed to the conceptualization.

Conflict of interest The authors declare that they have no conflict of interest.

Supplementary information Supplementary materials are available in the online version of the paper.

Jihan Jiang received his BSc degree from the South China Agricultural University in 2023. Currently, he is a graduate student in the General Ma Research Group at Shenzhen University. He is currently focusing on amorphous alloy porous HER catalysts.

Jiang Ma received his BSc degree in materials science and engineering from the Southeast University in 2009 and PhD degree from the Institute of Physics, Chinese Academy of Sciences (CAS) in 2014. He is currently a professor at the College of Mechatronics and Control Engineering, Shenzhen University, and received the Outstanding Teacher Award of Shenzhen in 2018. His research interest includes the formation, functional application and high-frequency dynamic loading behavior of metallic glasses

自支撑部分结晶纳米多孔金属玻璃催化电极实现高效制氢

蒋继汉[1], 阮文清[1*], 曾圣浩[1], 林嘉庆[1], 赵星然[1], 傅佳男[2], 陈庆[3], 刘晓俤[1*], 马将[1*]

摘要 金属玻璃(MGs)在中性和碱性介质中通常存在析氢反应(HER)动力学缓慢的问题, 其催化性能主要局限于酸性环境. 本研究报道了一种新型热塑性成型技术, 用于制备自支撑部分晶化纳米多孔$Pt_{56.2}Ni_{5.2}Cu_{16.8}P_{21.8}$金属玻璃(C-NPMG), 该材料展现出卓越的全pH值HER活性和长期耐久性. 在10 mA cm^{-2}电流密度下, C-NPMG催化剂表现出超低过电位: 酸性介质(0.5 M H_2SO_4) 18.0 mV、碱性介质(1 M KOH) 42.2 mV、中性介质(1 M PBS) 88.0 mV, 其性能优于大多数先进非贵金属MGs和Pt基催化剂. 值得注意的是, 该催化剂在碱性电解液中运行1000 h后性能衰减可忽略不计, 展现出卓越的稳定性. 实验与计算分析表明, 其优异的HER活性源于三重协同效应: (1) 高比表面积的纳米多孔结构最大化活性位点暴露; (2) 部分晶化过程中形成的微晶-非晶界面降低了H_2解吸能垒; (3) C-NPMG的分级超亲水-超疏水润湿性优化了传质过程并防止电解液腐蚀. 本研究通过将结构纳米工程与微晶-非晶相协同效应整合于金属玻璃体系, 为解决电化学水分解中性能与稳定性难以兼顾的难题建立了新型设计范式, 为开发高性能全pH值HER催化剂提供了新思路.